DSP-Based Link Tomography for Amplifier Gain Estimation and Anomaly Detection in C+L-Band Systems

Matheus Sena ⬤, *Graduate Student Member, IEEE*, Robert Emmerich ⬤, Behnam Shariati ⬤, *Member, IEEE*,
Caio Santos ⬤, Antonio Napoli ⬤, Johannes K. Fischer ⬤, *Senior Member, IEEE*, and Ronald Freund

(Invited Paper)

Abstract—**A successful migration from current C-band based optical networks to a multiband scenario primarily depends on the development of solutions that can reliably measure physical properties of optical links over broad spectral transmission windows. Additionally, these solutions must be capable of delivering wavelength-dependent and spatially-resolved indicators that can empower network operators to identify faults before they lead to severe service disruptions. Recently, the exploitation of receiver based digital signal processing as a tool for optical performance monitoring has gained tremendous popularity. One successful example is the so-called *in-situ* power profile estimator, which can reconstruct the per-channel longitudinal power profile along the optical fiber link solely processing the received signal samples. In this work, we propose a novel application for the *in-situ* power profile estimator by harnessing it on multiple wavelengths to accurately estimate the spectral gain profile of C+L-band in-line Erbium-doped fiber amplifiers deployed in a 280-km single mode fiber link. Furthermore, we show how this scheme can be efficiently used to detect amplification-related anomalies, such as gain tilt and narrowband gain compression. In our measurements, we achieved a sub-dB estimation accuracy by comparing the proposed gain extraction approach with the back-to-back characterization obtained from an optical spectrum analyzer.**

Index Terms—**Anomaly detection, C+L-band, digital signal processing, fiber nonlinearity, optical performance monitoring.**

Matheus Sena, Robert Emmerich, Behnam Shariati, Caio Santos, Johannes K. Fischer, and Ronald Freund are with the Fraunhofer Institute for Telecommunications Heinrich-Hertz-Institute, 10587 Berlin, Germany (e-mail: matheus.sena@hhi.fraunhofer.de; robert.emmerich@hhi.fraunhofer.de; behnam.shariati@hhi.fraunhofer.de; caio.santos@hhi.fraunhofer.de; johannes.fischer@hhi.fraunhofer.de; ronald.freund@hhi.fraunhofer.de).

Antonio Napoli is with Infinera, 81541 Munich, Germany (e-mail: anapoli@infinera.com).

I. INTRODUCTION

AS OF January 2021, a number of 4.66 billion Internet users was estimated worldwide, corresponding to approximately 59% of the global population [1]. By connecting billions of people, the Internet has become a core pillar of modern society and living without it is currently unimaginable. Despite the Internet's diffused penetration across the globe, the increasing demand for high-bandwidth applications requires enhanced network infrastructures capable to support high data speeds and demanding data consumption habits. To illustrate, during the 2020/2021 COVID-19 pandemic, remote work applications, teleconferencing, and video-on-demand platforms have increased traffic up to 200% at peak hours [2]. In these extreme scenarios, optical networks play a fundamental role in providing reliable Internet operation since 95 % of the Internet data traffic is transferred over optical fiber cables [3]. Therefore, one of the main concerns for operators is the realization of innovative approaches that permit to reutilize the already deployed optical fiber infrastructure, increasing the achievable capacity and avoiding traffic congestion. A promising solution is the deployment of the optical multiband (MB), or ultra-wideband (UWB), wavelength-division multiplexing (WDM) systems [4]. The main goal of optical MB systems is to extend the current standard optical transmission window ($\sim$5 THz, C-band) by aggregating neighboring bands (O-, E-, S- and/or L-band) leading to additional $\sim$50 THz of bandwidth compared to conventional C-band systems.

A secure migration from today's C-band based optical networks to a MB scenario heavily relies on monitoring mechanisms that can accurately measure not only wavelength-resolved characteristics of MB optical components (e.g., amplifiers [5], switches [6], [7], and transceivers [8]) but also distance-wise properties of optical links across nationwide networks. That is relevant because these monitoring capabilities will support MB network provisioning strategies [9] in multiple of the nowadays' challenges, for instance, reducing uncertainties about physical layer parameters [10], discovering types of fiber deployed in the link [11], assertively identifying origin of transmission faults [12]. However, despite the variety of optical performance monitoring (OPM) techniques and devices traditionally

employed in current commercial optical systems, a central and open question in the optical communication community is: how to efficiently distribute monitors across complex networks in a cost-effective way in order to capture wavelength-resolved, spatially-distributed information [13]? Recently, several monitoring features have been obtained by solely exploiting receiver (Rx) digital signal processing (DSP) modules [14]–[18], thus minimizing the requirements of distributed node-level measurement devices. The popularity of these Rx-based OPM approaches is due in part to their capability of unveiling multi-span link properties, such as longitudinal power profile [14], [15], frequency response of bandpass filters [16], span-wise chromatic dispersion mapping [17] and Raman gain [18]. One successful example of such application was introduced in [14], where the authors proposed an *in-situ* power profile estimator (PPE) that reconstructs the channel power evolution along the link with sub-km resolutions [15]. An insightful application that we foresee from this technique is that by overlaying the *in-situ* PPE from multiple WDM channels it is possible to create a distance-wise, wavelength-dependent link tomography [13]. This link tomography embodies the relation power versus wavelength versus distance and discloses multi-degree characteristics of the optical link, later explored in this text.

In this contribution, we experimentally investigate the application of a Rx-DSP approach (hereafter named link tomography) to extract the spectral gain profile of C+L-band Erbium-doped fiber amplifiers (EDFA)s and detect soft-failures, such as gain tilt and narrowband gain compression. The construction of the link tomography is based on the utilization of the *in-situ* PPE [14], [15], which is *per se* a suitable approach for any optical band (including the traditional C-band), but has been specifically used in this work for C+L-band systems. This is demonstrated by running a single-channel experimental campaign in a C+L-band setup over 280 km of single mode fiber (SMF). In this study, we extend our previous contribution presented in [19] by:

1) deepening the level of technical discussions on the underlying principles that permit us to use the Rx-DSP as a monitoring tool in MB systems;
2) including additional simulative analysis on the limitations and opportunities that can be explored from the link tomography;
3) introducing a new scenario for soft-failure detection, where the algorithm can capture narrowband gain compression caused by spectral-hole burning (SHB) based effects.

Particularly, the link tomography is a major feature in at least two important contexts in the field of optical communications. First, it can be used in cognitive optical networks [19]. This is possible because the device (in this case the receiver) can "sense" events in the link, such as the appearance of gain tilts, and be used to trigger automatic decisions carried out by a network controller. Second, it has an additional applicability in the context of partially disaggregated network systems [21], for which terminals operate over multi-vendor networks and infrastructure information cannot always be shared. This means that the link tomography can be utilized as a mapping tool that characterizes in-line components regardless of the availability of information provided by vendors.

The remainder of this text is structured as follows. Section II briefly summarizes other related works and clarifies this manuscript's position among them. Section III introduces the working principles of the link tomography and analyzes opportunities and limitations of the technique through simulations. Section IV assesses the experimental outcomes of the link tomography to extract the spectral gain of optical amplifiers and to detect soft-failures. Finally, the main conclusions and considerations of this work are summarized in Section V.

II. RELATED WORK

OPM plays a decisive role in diagnosing the health of optical communication systems. However, collecting measurements from multiple nodes across complex networks is a challenging and costly task. To overcome this issue, disruptive solutions were recently devised to obtain as much information as possible from the optical link by means of Rx-DSP, i.e., without deploying additional measurement equipment (e.g., optical time-domain reflectometer (OTDR)). In this context, fiber-longitudinal monitors have been demonstrated using adaptive digital backpropagation (DBP) algorithms, where the fiber parameters are optimized to fit the actual reality of the transmission link [22]. For instance, by estimating the segment-wise nonlinear phase rotation (NLPR) caused by the Kerr effect, it is possible to indirectly measure the longitudinal power evolution along the fiber link [16] and, consequently, identify anomalous attenuation points [17]. Alternatively, these methods can be also applied to visualize chromatic dispersion coefficient and help discriminate span-wise types of fibers [17]. Numerical complexity is still one of the main drawbacks of these approaches as they can lead to an N-dimensional optimization problem (where N is the number of fiber segments), which becomes even more difficult to be solved when no *a priori* link information is available. To overcome this difficulty, the authors in [14] proposed a simplified DBP to extract the value of the optical power at any specific spatial location along the transmission path. This method, the *in-situ* PPE, does not require resource-demanding optimizations and can indicate link properties (e.g., attenuation profile) and anomalous events (attenuation points) with impressive sub-km resolutions [15].

One possible application of the *in-situ* PPE is the construction of a distance-wise, wavelength-dependent link tomography. In this scheme, the longitudinal power profiles of multiple WDM channels are overlaid to enable a spatially- and wavelength-resolved visualization of the channels' power evolution. This feature is crucial for MB systems as power-related, wavelength-dependent physical properties of fiber links can be directly estimated from the link tomography. For instance, in [18] the authors showcase a tomography-like approach that is able to reveal the Raman spectral gain of individual distributed Raman amplifiers. In a similar way, we demonstrate in this work that the link tomography can be also used to disclose the spectral gain of C+L-band EDFAs and help discover soft-failures in these devices, such as anomalous gain tilts [23] and narrowband gain compressions caused by SHB [24].

TABLE I
SUMMARY OF RELEVANT WORKS CONCERNING RX-DSP OPM APPROACHES

| Method	Discovered link property	Discovered link anomaly	Reference
In-situ PPE	Longitudinal power profile	Identification of excessive attenuation points	[14]
In-situ PPE	Longitudinal power profile	Accurate location of excessive attenuation points	[15]
Adaptive DBP	Longitudinal power profile; Frequency response of bandpass optical filters;	Narrowband filtering	[16]
Adaptive DBP	Span-wise chromatic disperison coefficient	Identification of excessive attenuation points	[17]
Adaptive DBP	Spectral gain of distributed Raman amplifiers	-	[18]
In-situ PPE	Spectral gain of C+L-band EDFAs	Gain tilt and narrowband gain compression	**This work**
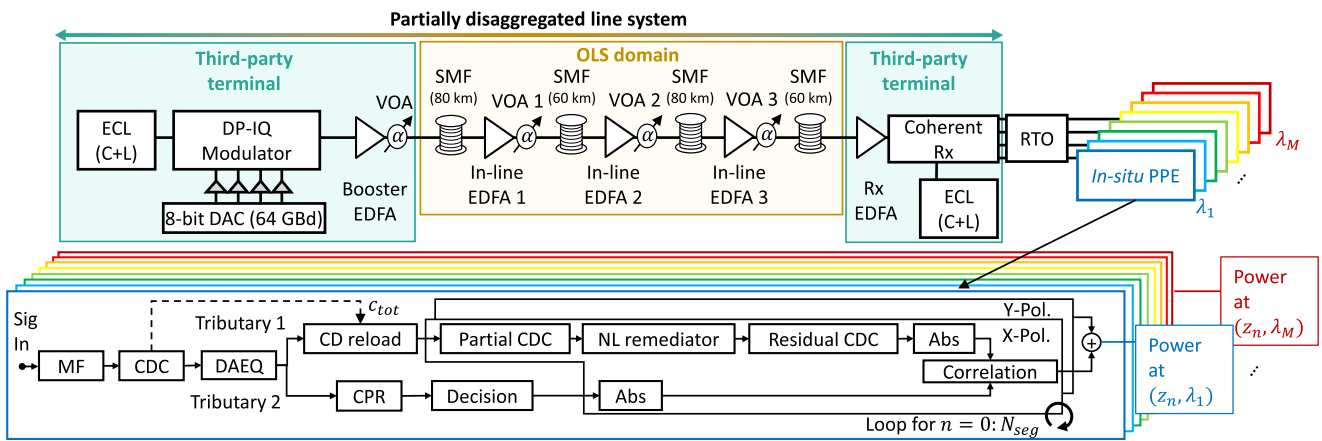
Fig. 1. Experimental setup and Rx-DSP scheme used in the link tomography. By overlaying the output of the *in-situ* PPE from multiple WDM channels, depicted by the wavelengths λ_1-λ_M, one can build a link tomography that visualizes the wavelength- and distance-resolved power evolution of the link. VOA: Variable optical amplifier. Abs.: Absolute value of the signal samples.

Table I summarizes other related works with respect to discovered link properties and anomalies. We emphasize that our study is, to the best of our knowledge, the first to: (1) validate the use of the *in-situ* PPE for optical MB systems (C+L-band); (2) demonstrate a terminal-side estimation of the gain of each individual EDFA deployed in an open line system (OLS); (3) utilize the receiver DSP to identify two types of faults in EDFAs, namely, gain tilt and gain compression due to SHB.

III. LINK TOMOGRAPHY

1) Working Principle: In this work, we propose a link tomography, which is inspired by the *in-situ* PPE proposed by T. Tanimura *et al.* in [14]. Strictly speaking, the principle described in this paper is "inspired" by [14] because, from the algorithmic point of view, slight changes (later explained in this text) were accommodated into our custom implementation. In spite of that, the core principle of the technique presented in [14] remains untouched and, for that reason, we take the liberty to refer to our implementation as inspired by the *in-situ* PPE. Although this section's discussion provides a brief description about the *in-situ* PPE, for an in-depth analysis of the method we highly recommend the reading of the contribution referenced in [15] and published in this journal.

The core concept of the *in-situ* PPE is to develop a monitor that delivers a per-channel longitudinal power profile along the fiber link. This is possible thanks to the non-commutative relationship between the chromatic dispersion and the nonlinear interference induced by the channel on itself, i.e., self-phase modulation (SPM). This non-commutativity permits that characteristics of the channel, through which the signal propagates, be uniquely determined by applying a reverse-order operation. Then, at the Rx-DSP, one can estimate channel properties from the digitized samples by using a relatively simple DSP chain, which is shortly explained as follows.

To begin, let us consider the setup shown in Fig. 1, which can be abstracted as a partially disaggregated system comprised of an OLS and third-party terminals. For now, we concentrate our discussion on the Rx-DSP (Fig. 1, bottom) and leave the explanation about the component-level specificities of the setup for sub-section IV.1. After the reception of the optical signal by a coherent receiver, the four quadrature components, i.e., X (horizontal polarization) / Y (vertical polarization) in-phase (I) and X/Y quadrature (Q), are digitized with a real-time oscilloscope (RTO). A matched filter (MF) followed by a blind chromatic dispersion compensator (CDC) block are applied to the output signal from the RTO, i.e., Sig In. Then, a data-aided equalizer (DAEQ) block for polarization demultiplexing and frequency

offset correction is used at the output of the CDC. At this stage, the resulting signal is split up into two tributaries, i.e., Tributary 1 and Tributary 2, where the former is used in a simplified DBP, while the latter in a recovery process that attempts to recreate a version of the signal before the link propagation. For that purpose, both Tributaries are processed in different and independent DSP chains.

The initial stage of the Tributary 1 DSP chain consists of reloading the total chromatic dispersion (c_{tot}), which was previously estimated by the CDC block. After that, the two polarizations (X/Y-pol) of the signal are separately treated by a three-step iterative process, which consists of: 1) a partial CDC; 2) nonlinear (NL) remediator; and 3) a residual CDC. At the partial CDC, each polarization is compensated for chromatic dispersion (CD) by a value of $n \times c_{tot}/N$, where n is an integer number corresponding to the index of the fiber segment, i.e., $n = 0, 1, 2, \ldots, N$, and N is the total number of fiber segments in the link. Therefore, a CDC of $n \times c_{tot}/N$ corresponds to partially accounting for the CD of n fiber segments. As for the NL remediator, this block attempts to compensate for any point-wise nonlinear phase noise due to the Kerr effect. This is achieved by applying the following fixed formula onto the outgoing channel from the partial CDC:

$$u_{out,\mathrm{X/Y}}[k] = u_{in,\mathrm{X/Y}}[k]$$
$$\exp\left(-j\varepsilon\left(|u_{in,\mathrm{X}}[k]|^2 + |u_{in,\mathrm{Y}}[k]|^2\right)\right) \quad (1)$$

where u_{in}/u_{out} is the digital representation of the input/output complex-valued electric field, k is the sample index and ε is a fixed hyperparameter. It is important to note that, as emphasized in [15], ε should be set to a fixed value. In this work, we assumed it to be $\varepsilon = 0.004$, which is in the same range of the value assumed in [15]. Finally, the residual CDC is applied. This block is equivalent to correcting the CD of the $N - n$ segments of fiber, which translates into a CDC of $c_{tot} - n \times c_{tot}/N$.

For the signal Tributary 2, as mentioned before, we apply a standard receiver DSP chain to recover the signal to an as-close-as-possible representation of the transmitted signal. In this work, this DSP chain only consists of carrier phase recovery (CPR) and a decision based on the nearest constellation symbol, as the other needed blocks were part of the previous stage.

Finally, to obtain a quantitative indicator of the signal power at a distance z_n (w.r.t the receiver side), we calculate the correlation between the processed Tributary 1 and 2 and sum up the results from each polarization. To construct the full longitudinal power profile, i.e., the output of the *in-situ* PPE, the above-described procedure must be looped for $n = 0, 1, 2, \ldots, N_{seg}$. For each loop iteration, a fixed number of 2^{15} symbols is used in the DSP chain of Tributary 1. Here, we emphasize that the Tributary 2 DSP chain could be further enhanced with the use of sophisticated forward-error correction (FEC) mechanisms in order to improve the symbol decision. Another possibility is to realize the averaging of multiple *in-situ* PPE outputs to minimize the effect caused by possible wrong symbol decisions. In the results obtained in this work, each *in-situ* PPE curve used to build the link tomography was averaged for at least 8 times.
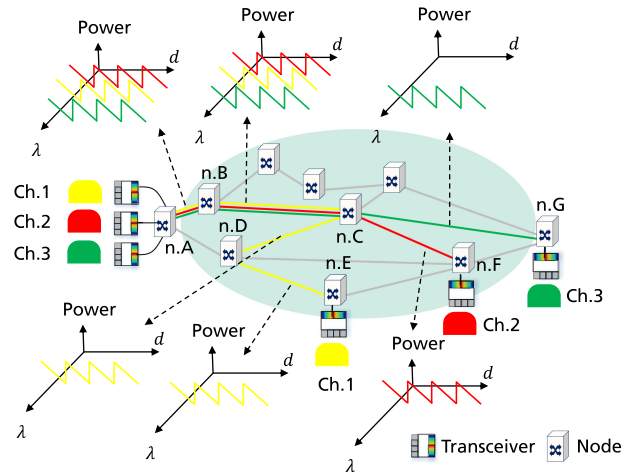

Fig. 2. In a networkwide tomography, the estimated channel's power profile for the entire route must be split into link-based segments and only overlaid with the co-propagating channels that share the same link. Ch.: Channel.

In this work, slight algorithmic changes in the *in-situ* PPE were implemented in comparison to the version introduced in [14]. First, in our approach the algorithm is applied to the entire block of 2^{15} DAC-generated symbols, which, in contrast to [14], means that we do not sub-divide this sequence into smaller data processing blocks at the receiver DSP. Second, this alteration permits us to allocate the MF block outside of the iterative loop depicted in Fig. 1, and avoids repeating the filtering of the same signal for each loop iteration. In our study, we found it to improve the computational time. Although these changes slightly distinguish our implementation to the one proposed by Takahito *et al.*, they do not translate into a concept modification. We believe that the main innovation presented in this work goes beyond any algorithmic customization. Rather, it is the introduction and validation of the concept of link tomography that, unlike the related works (Table I), permits to extract the gain profile of EDFAs in C+L-band scenarios and identify amplifier faults, e.g., gain tilt and gain compression.

Now it is clear that when applying the *in-situ* PPE on each WDM channel, depicted in Fig. 1 by the wavelengths λ_1-λ_N, it is possible to create a wavelength-resolved and distance-wise visualization of the power profile along the link, which has been named link tomography.

The link tomography is the first obvious step towards the design of a networkwide tomography [13]. In this network-level design, however, frequency continuity along the same route is not a reality as optical channels can be added/dropped at intermediate nodes. This means that, in a networkwide tomography, the estimated channel's power profile for the entire route should be split into link-based segments and only overlaid with the co-propagating channels that share the same link. The aggregation of all link tomographies would then permit us to appropriately visualize the power characteristics in complex topologies. To illustrate, let us assume the scheme shown in Fig. 2, where channels 1, 2 and 3 depart from the same terminal side, i.e., node A (shortly n.A), and travel together up to n.C,
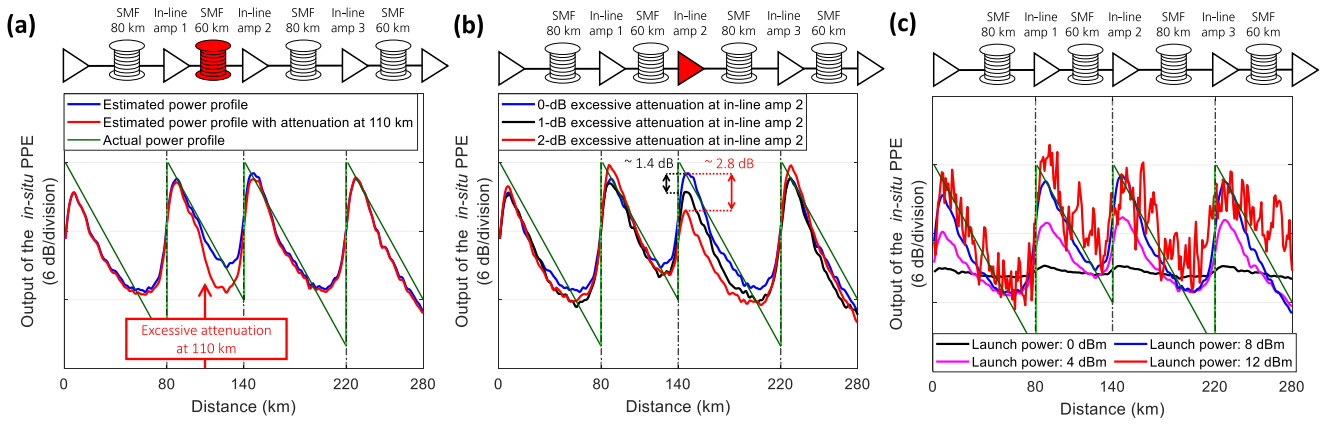
Fig. 3. (a) Result of a simulative analysis for validation of the *in-situ* PPE without (blue curve) and with an excessive fiber attenuation point at 110 km (red curve). (b) Output of the *in-situ* PPE when the gain of in-line amplifier 2 (highlighted in red in the link schematic) is attenuated by 1 and 2 dB (black and red curve, respectively). (c) Output of the *in-situ* PPE when four launch power regimes, i.e., 0, 4, 8 and 12 dBm, are evaluated. Amp.: amplifier.

from which they follow independent trajectories to n.E, n.F and n.G, respectively. When the *in-situ* PPE is applied to channels 1, 2 and 3, we can obtain the power visualization across the routes n.A-n.B-n.C-n.D-n.E, n.A-n.B-n.C-n.F and n.A-n.B-n.C-n.G, respectively. However, due to the spectral non-continuity of these channels after n.C, a link-based sectioning of the power profile is necessary, as shown in Fig. 2. This segmentation would then exclude the need of dedicated pairs of transceivers per link. Another important aspect to consider in a network scenario, is that nodes can induce effects such as narrowband filtering. Although the implication of this impairment is not investigated in this work, similar Rx-based OPMs methods can help account for it and deliver accurate power estimations [16].

2) Simulative Analysis: Before diving into the experimental aspects of the link tomography, it is important to assess the method via numerical simulations and outline opportunities and limitations of the *in-situ* PPE. The simulations have been carried out with the commercial tool *VPItransmissionMaker^{TM}* using the *VPItoolkit DSP-Library*. In this simulative analysis, the *in-situ* PPE is evaluated to estimate the single-channel power evolution of a dual-polarization (DP) 16 quadrature-amplitude modulation (QAM) signal at a symbol rate of 64 GBd, which is transmitted over 280 km of SMF. The link is similar to the setup shown in Fig. 1, i.e., it consists of 2×80-km (1st and 3rd spans) and 2×60-km spans (2nd and 4th spans). The fiber properties (e.g., fiber attenuation: 0.2 dB·km^{-1}, chromatic dispersion coefficient: 16.5 ps·nm^{-1}·km^{-1} and nonlinear coefficient: 1.07 W^{-1}·km^{-1}) are constant for all four spans. All amplifiers, i.e., the terminal and in-line, are identical and provide a fixed output power of 8 dBm with a noise figure of 5 dB. The numerical simulations are implemented via the split-step Fourier method with a step size of 1 km and a simulation bandwidth of eight times the symbol rate of the tested signal. For the *in-situ* PPE, we considered N = 280, i.e., each fiber "virtual" segment in the algorithm has a length of 1 km.

In Fig. 3a, illustrated by the blue curve, we find the output of the *in-situ* PPE obtained in our simulation. Here we observe that a good agreement is achieved between the estimated signal power evolution and the actual power profile, which

was retrieved from the simulation (green solid lines). Another interesting aspect is to check whether the scheme can capture anomalous attenuation "events" in the link. This is performed with the inclusion of a 3-dB attenuation point at 110 km. As one can notice, the new output of the *in-situ* PPE (red curve in Fig. 3a) follows a similar behavior, w.r.t. the blue curve, up to the location of the attenuation point (at 110 km), where it detaches and plunges very rapidly. This shows the capability of the method in identifying power-related soft-failures present in the link. In a similar way, the scheme can be used to visualize variations in the gain of the amplifiers, which is investigated in the results shown in Fig. 3b. In this case, we attenuate the gain of the in-line amplifier 2, highlighted in red in the link schematic on top of Fig. 3b, by 1 and 2 dB. This gain variation can be directly visualized in Fig. 3b by the three distinct readings of power levels provided by the in-line amplifier 2 in the vicinity of the 140th km. As also shown in Fig. 3b, the difference between the peaks of the blue and the black curve is approximately 1.4 dB, whereas the difference between the peaks of the blue and red curve is 2.8 dB. The possibility to visualize gain variations is a very important feature that will be further explored in Section IV and comprises one of the main properties of the *in-situ* PPE that motivates the novel application introduced in this work.

Although the *in-situ* PPE can be used as a relatively good mapping tool for coherent optical transmission systems, there are still some limitations that must be considered. For instance, this technique has restricted capability in either very high or very low power regimes. To exemplify this, we use the results shown in Fig. 3c, where the output power of all amplifiers in the link is set to four possible levels, namely, (1) 0 dBm, (2) 4 dBm, (3) 8 dBm and (4) 12 dBm. This means that the single-channel power can assume one of the four mentioned values (0, 4, 8 and 12 dBm). In (1), which is depicted by the black curve in Fig. 3c, we see that the reading of the power profile is vertically compressed and that the monotonically decreasing profile caused by the fiber attenuation cannot be easily detected. This can be explained by the fact that, at lower power regimes, the signal is dominantly impaired by the amplified spontaneous emission (ASE) noise generated by the amplifiers. Therefore, the SPM becomes overshadowed by this

linear effect and, consequently, the estimation of the power at a given distance is hindered. As we move to higher launch powers, e.g., (2) 4 dBm (magenta curve) and (3) 8 dBm (blue curve), the reading of the power profile becomes clearly visible along the link, which means that the signal nonlinearity is already sufficient to enable the path monitoring. Intuitively, one could think that the progressive increase of the launch power would lead to an improved estimation of the profile once the *in-situ* PPE is only possible thanks to the nonlinear characteristics of the fiber. However, as shown by the red curve in Fig. 3c, a launch power of 12 dBm yields a highly distorted estimation of the profile. A likely explanation for this is that the fiber nonlinearity is now so dominant to the extent that it impairs the signal and does not permit the reconstruction of the reference signal through the DSP chain used for Tributary 2. Consequently, an inaccurate power profile estimation is obtained.

Another important aspect to consider is the presence of co-propagating channels. Since the *in-situ* PPE relies on an accurate estimation of the SPM, any additional influence of adjacent channels, i.e., cross-phase modulation (XPM), may contribute to a degradation of the power estimation. To study the effect of XPM, we compare the *in-situ* PPE in two different transmission scenarios: single- vs. multi-channel. In the latter, we simulated a C+L-band transmission, where each band is composed of 31 channels (DP-16QAM, 64 GBd) and the longitudinal power estimation is acquired from the center channels in the C- and L-band, i.e., at 1551 nm and 1579 nm, respectively. To avoid an excessive total launch power into the fiber, while still permitting that some channels have enough power to possibly reconstruct a link tomography, we considered the following per-band power distribution: 7×5-dBm channels (including the center channel) $+ 24 \times 0$-dBm. Between every two consecutive 5-dBm channels, there are three 0-dBm channels, as depicted in the spectral representation in Fig. 4d. By interleaving high-power with low-power channels, one can manage the total power launched into the fiber, which becomes a limiting factor as the spectral loading increases. In this new simulation, we considered the same fiber parameters used in the previous results (Fig. 3(a), (b)) and a simulation bandwidth of 160 times the symbol rate of the tested signals. In Fig. 4c, we see some degradation of the obtained power profile for the multi-channel case in comparison to the single-channel transmission (Fig. 4a). Yet, it is undeniable that the nature of the estimated power profile is still very visible and with a relatively good agreement to the single-channel extraction. Of course, this degradation can vary depending on multiple factors, e.g., spacing between channels, power of channels, number of channels. Although we have not fully assessed the impact of all these factors in the multi-channel scenario, the presented results are a proof-of-concept that the proposed link tomography can be applied in such scenarios. Moreover, its performance can be possibly improved, which will be the focus of our future research endeavors.

As already noted, the *in-situ* PPE can capture the nature of longitudinal, power-related properties of the link when certain criteria are respected. This means that when applied on multiple WDM channels, this technique will embody the wavelength-dependent characteristics of the power evolution and can be used
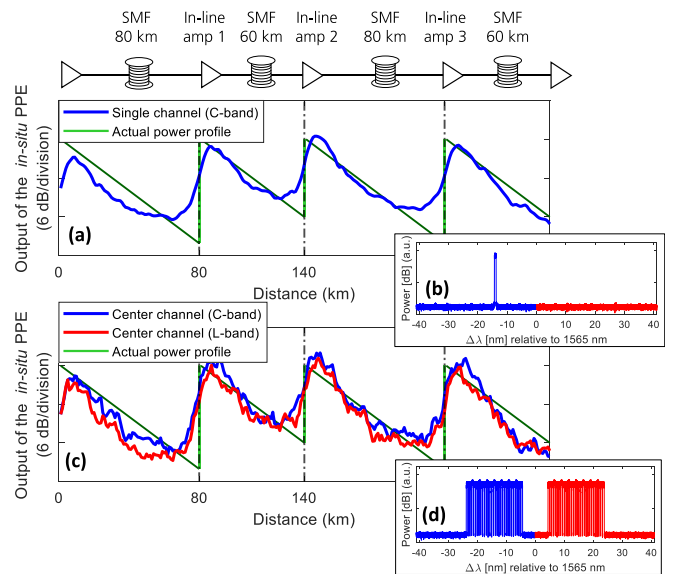

Fig. 4. (a) Output of the PPE for a C-band single-channel transmission. (b) Spectrum of the transmitted channel (single-channel scenario). (c) Output of the PPE for a C- and L-band channel in multi-channel transmission. (d) Spectrum of the transmitted channels (multi-channel scenario).

to estimate the power behavior along the wavelength domain. This is a key feature in the context of MB systems since it enables to discover properties such as MB spectral gain of the in-line amplifiers and spot faults in their operation (e.g., gain tilts). In the next sub-section, we showcase how this was achieved in this work.

IV. DISCUSSION

1) Experimental Setup: To explain the experimental testbed used in this work, we ask the reader to revisit the scheme shown in Fig. 1. As depicted, the transmitter is composed by a 4-ch 84 GSa/s DAC and a commercial C-band optical multi-format transmitter comprising a quad-set of driver amplifiers and a LiNbO$_3$-based DP IQ-modulator. To account for MB component-induced impairments [25], we applied Volterra-based digital pre-distortion (DPD) as it has been proven to be a successful way to boost b2b performance in S+C+L-band systems [25]. Therefore, in our experiment we characterized the transmitter with a truncated, time-invariant 3rd-order Volterra series (256 taps in the first order, 9 taps in the second and third orders) and utilized this model to create a Volterra-based DPD filter, which was synthesized using indirect learning architecture [27]. In the sequence, this DPD filter was applied on a 64-GBd DP-16-QAM signal generated with a 2^{15} pseudo-random bit sequence and shaped with a root-raised cosine pulse filter (roll-off factor 0.1). Additionally, a chromatic dispersion pre-compensation of 800 ps/nm was digitally added to the signal (as suggested in [15]), which was transmitted over a 280-km SMF link.

Given that this was a single-channel experiment, to emulate the multiple WDM channels we utilized two tunable external
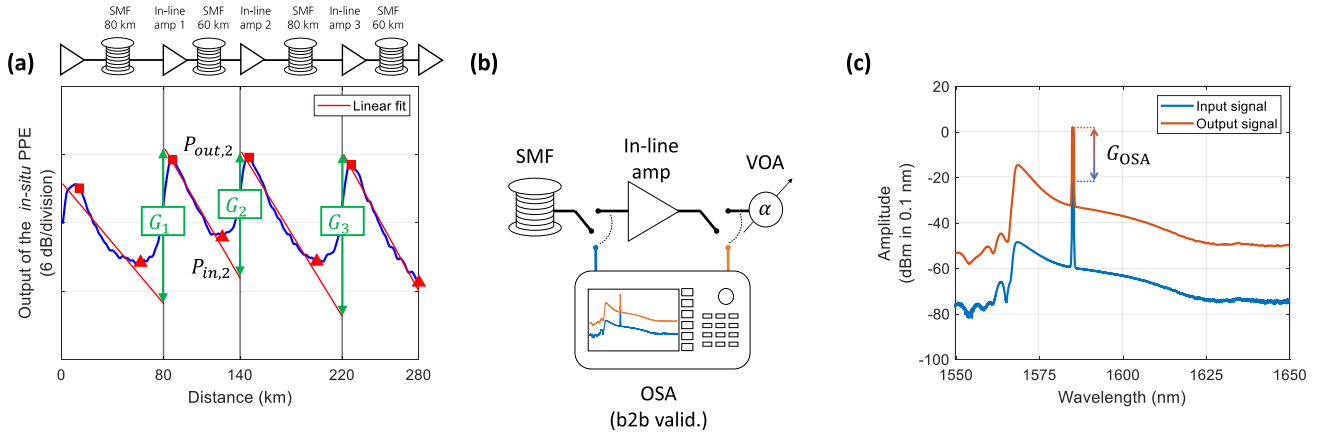
Fig. 5. (a) Longitudinal power profile (blue curve) and span-wise linear fits (red curves) used to estimate the gain G_i (for a fixed wavelength) of the i-th in-line amplifier. For instance, by subtracting $P_{in,2}$ from $P_{out,2}$, it is possible to estimate G_2. b) Scheme to perform the b2b validation of the in-line amplifier gain. In this scheme, the input and output power spectrum densities are measured and subtracted to estimate G_{OSA} (for fixed wavelength). (c) Example of input and output spectra, when the channel's central wavelength is 1585 nm.

cavity laser (ECL) sources as means to cover the tested wavelengths in the C- (1527.5 – 1565 nm), and L-band (1570 – 1600 nm). The ECLs were set to a constant output power of approximately 16 dBm. The investigated link consists of two 80-km (1ˢᵗ and 3ʳᵈ span), and two 60-km (2ⁿᵈ and 4ᵗʰ span) SMF spans. All EDFAs (terminal and in-line) were operated in the intervals of 1540 – 1565 nm (C-band) and 1570 – 1605 nm (L-band) while running in the automatic current control (ACC) mode, for which maximum currents of 350 mA, in the C-band, and 700 mA, in the L-band, were set. After the signal was received by a coherent receiver (70 GHz of bandwidth), it was digitized by a 200 GSa/s RTO (8-bit resolution, 70 GHz of analog bandwidth) and followed by the Rx-DSP chain already detailed in sub-section IV.1.

Finally, the emulation of the multiple WDM channels was performed by sweeping the ECL central wavelength in steps of 2.5 nm. For each tested wavelength, the *in-situ* PPE was executed, averaged and, at the end of this sweeping process, the link tomography was built.

2) Spectral Gain Estimation: As previously mentioned, in the first application derived from the link tomography we planned to measure the spectral gain of the in-line amplifiers. This is possible because the link tomography can be used to estimate (for each tested wavelength) the input ($P_{in,i}$) output ($P_{out,i}$) power of the i-th in-line EDFA. Consequently, the difference between these two values (in dB) yields the gain of the amplifier, denoted by G_i. To improve the estimations of G_i, we found appropriate to use a simple linear fit, i.e., $a\mathbf{x} + b$, on the monotonically decreasing segments of the power profile curve. To give an example, if we assume the simulative scenario used in the previous section, $\mathbf{x}$ is the span-wise set of distance points between the maximum (square-like markers in Fig. 5a) and minimum values (triangle-like markers in Fig. 5a) obtained from the *in-situ* PPE. As for the constants a and b, these are scalar values to be optimized such to minimize the mean squared-error between the linear fit and the power profile curve. Illustratively, these linear fits correspond to the

red curves shown in Fig. 5a. After that, it becomes simple to estimate $P_{in,i}$ and $P_{out,i}$, as exemplified for $P_{in,2}$ and $P_{out,2}$ in Fig. 5a. It is important to highlight that this procedure is just a low-complexity engineering strategy that we utilized to reduce uncertainties of determining G_i. It should be stressed that the construction of the link tomography itself is not dependent on this mathematical manipulation.

To measure the spectral gain of the in-line EDFAs, we defined two gain characterization methodologies: (1) *commissioning* and (2) *operation* modes. By *commissioning* mode, we imply that the spectral gain of the i-th amplifier under test (AUT) is obtained for a constant input power (- 8 dBm in this work). Since the input power into the AUT is wavelength-dependent, in the *commissioning* mode it is necessary to tune the VOA of the $(i-1)$-th span, such to maintain a constant input power into the i-th amplifier whenever a new wavelength is set. The advantage of this approach is that the gain characterization is independent of the link configuration, i.e., it is inherent to device. However, the *commissioning* mode is only suitable for green-field applications, where the link can be unrestrictedly calibrated without interrupting transmission. As for the *operation* mode, the gain is measured without manipulating the VOAs in the link. This means that the spectral gain is measured regardless of the input power into the AUT. The advantage of this approach is that it indicates the effective gain imposed by the AUT on each WDM channel. Consequently, this methodology is more appropriate for a continuous link monitoring because it does not imply interruption of the transmission. Both methodologies were benchmarked against the back-to-back (b2b) validation depicted by the schematic in Fig. 5b. This means that we used the optical spectrum analyzer (OSA) to measure the input and output power at each AUT and directly obtain the gain (G_{OSA}). Fig. 5c shows the power spectrum densities of the input and output signals of the AUT 1 obtained from the OSA when the channel central wavelength is 1585 nm.

We stress that in our experimental setup it was necessary to add variable optical attenuators (VOA)s at the output of the
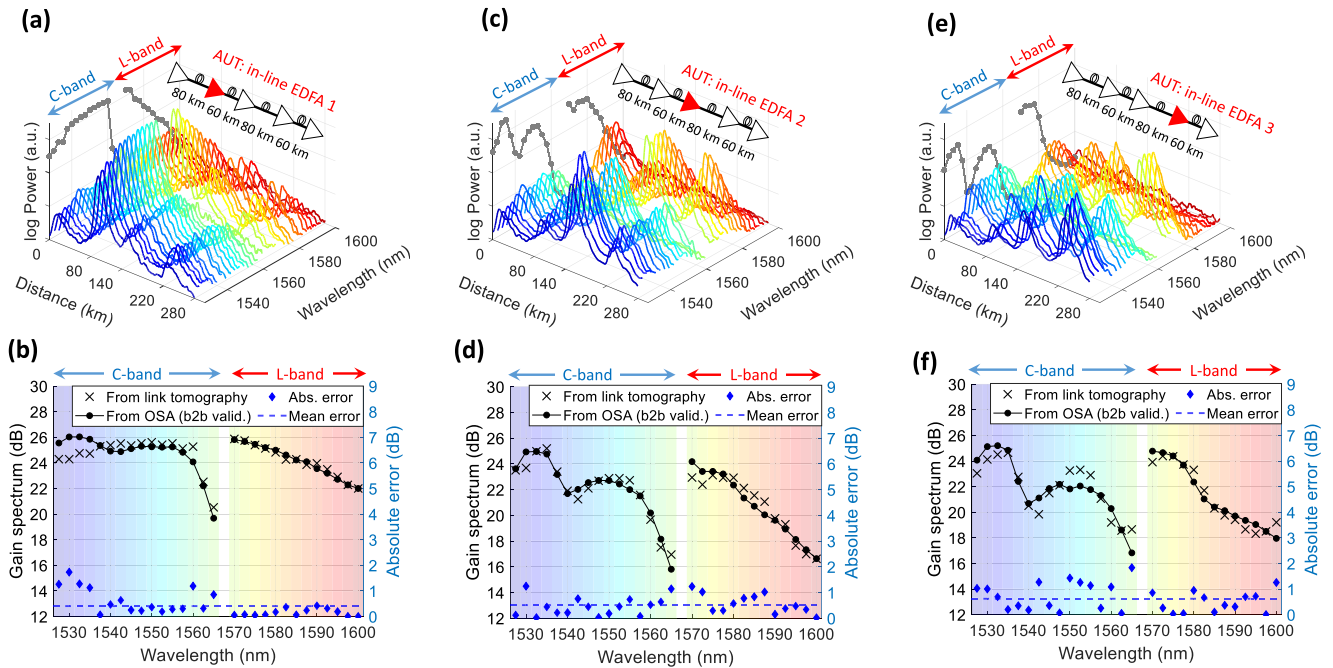
Fig. 6.   Link tomography used to estimate the spectral gain profile in the *commissioning* mode (constant input power of - 8 dBm) when the AUT is the in-line EDFA (a) 1, (c) 2 and (e) 3. To improve readability, in (a) (c) (e) We project the peak power estimated by the link tomography of the in-line EDFA 1, 2 and 3, respectively, onto the plane parallel to the wavelength axis. Estimated gain spectrum for the in-line EDFA (b) 1, (d) 2 and (f) 3.

EDFAs to avoid a high input power into the fiber. This would prevent, for instance, a distorted reading of the power profile such as the one shown by the red curve in Fig. 3c. Therefore, the link tomography always delivers the resulting gain of the two devices, i.e., EDFA + VOA. To extract the exact gain of the amplifier, we add a positive term A_i VOA to G_i to account for the attenuation of the i-the VOA, which is constant for each EDFA and known *a priori*. We emphasize that this procedure is only needed to accommodate the fact that in our testbed the EDFA and VOA virtually behave as a single device.

The results in Fig. 6(a), (c), (e) show the link tomography obtained in the *commissioning* mode when the AUT is the in-line EDFA 1, 2 and 3, respectively. The multiple curves that compose the link tomography (color-coded from dark blue to dark red) consist of the longitudinal power profile experienced by each WDM channel at the tested wavelengths in the C- and L-band. This explains the presence of four major spikes along the distance axis, which correspond to the amplification of the Booster EDFA and in-line EDFAs 1, 2 and 3. For instance, let us concentrate on the amplification behavior of the AUT 2. In Fig. 6c, it is possible to see that the power peak provided by the AUT 2, which happens at around 80 km, has a nature that varies with the wavelength axis. To improve the readability, we project the power peak provided by the AUT 2 onto the plane parallel to the wavelength axis, which is depicted by the gray curve in Fig. 6c. In this figure, we can identify a maximum power level at ∼1535 nm, which is then followed by a sharp drop at 1542.5 nm. After that, the power follows a parabolic profile up to 1557.5 nm and sharply drops again until it reaches a minimum at 1565 nm. In the L-band, the amplification follows an ever-decreasing

profile as the channel central wavelength is increased towards 1600 nm.

When the b2b validation of the AUT 2 gain profile is carried out with the OSA, illustrated by the circle-like markers in Fig. 6d, it is possible to confirm the estimation acquired from the link tomography. This means that the C-band amplification has a 1535-nm peak, which is followed by a sharp power drop at ∼ 1540 nm and a parabolic profile up to 1557.5 nm, while the L-band is always decreasing in the direction of longer wavelengths. Finally, we measure the gain of the AUT 2 via the link tomography, which is indicated by the cross-like markers in Fig. 6d. It is evident that this technique can, with a relatively good agreement, capture the spectral gain profile of the AUT 2, which is validated by the similar behavior followed by the cross-like markers relative to the OSA characterization curve. Numerically speaking, we also ensure a good agreement by obtaining a mean absolute error value over all the wavelengths (blue dashed line) of approximately 0.5 dB.

When the same procedure is applied to the AUT 1 and AUT 3, as exposed in Fig. 6(b), (f), an error of nearly 0.4 and 0.6 dB can be achieved, respectively. As we did before, we project onto the plane parallel to wavelength axis in Fig. 6(a), (e) the power peak provided by the AUT 1 and AUT 3 (gray curves). The nature of the estimated relationship output power versus wavelength is also confirmed when contrasted against the gain characterization from the OSA.

The results shown so far concern the application of the *commissioning* mode, i.e., all gain curves in Fig. 6 were obtained while maintaining a constant input power (− 8 dBm) into the AUT. Now, we focus on the *operation* mode. In this new
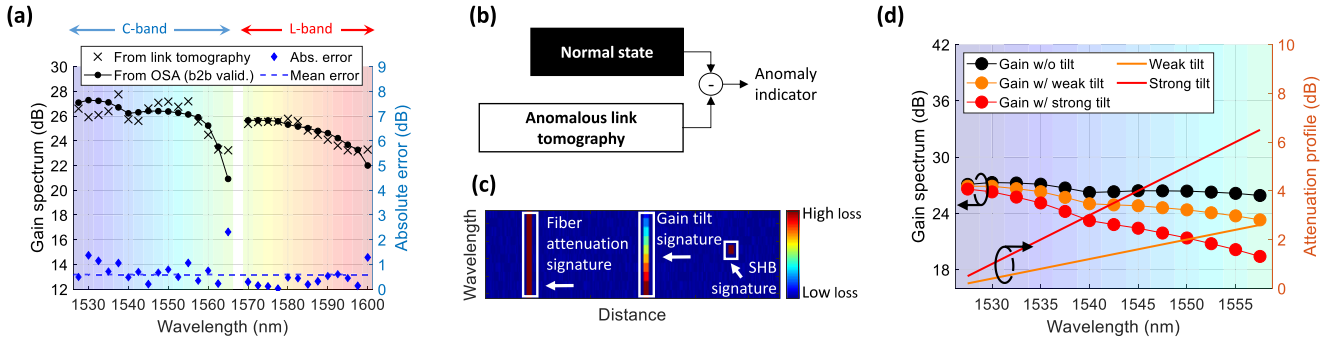
Fig. 7. (a) Estimated gain spectrum of the AUT 1 in the *operation* mode, i.e.., when no link manipulation is performed to maintain a constant input power. (b) Anomaly detection scheme used to detect gain tilt and narrowband gain compression due to SHB. (c) Anomaly indicator map distinguishing different types of faults. (d) Gain spectra of the AUT 1 without and with emulated gain tilts.

methodology, unlike in the previous mode, the VOAs are not manipulated to maintain a constant input power into the AUT, which is a more desirable characteristic for real-time monitoring of optical links.

To demonstrate the possibility of extracting the spectral gain in the *operation* mode from the link tomography, we depict the results from the in-line EDFA 1 in Fig. 7a. As it is possible to see, the spectral gain obtained from the link tomography has a good agreement with the b2b OSA validation, yielding a mean absolute error over all wavelengths of around 0.6 dB.

One additional feature that can be explored with the *operation* mode is the possibility to detect anomalies in the amplifiers, which is the topic of our next discussion.

3) Anomaly Detection in EDFAs: As demonstrated with the simulations shown in sub-section III.2, the *in-situ* PPE can detect attenuation events in the link. Consequently, this enables the link tomography to visualize wavelength-dependent effects that may degrade the signal power. One recurring fault in EDFAs that can be easily detected with the link tomography is the gain tilt. Gain tilts can significantly vary depending on channel-loading configurations and channel input power spectra [23]. In essence, a gain tilt corresponds to an imbalance of the spectral gain such that the amplifier loses its flatness, i.e., some channels are more amplified than others. This effect contributes to the cumulative degradation of the optical signal as it passes through multiple amplification stages, hence it is critical to track the evolution of gain tilts. In this work, we use a straightforward monitoring scheme to create an anomaly indicator and identify the occurrence of these effects. In this scheme, we simply perform the subtraction between a reference link tomography without anomalies (normal state) and the one with anomalies. The core idea is that the reference link tomography can be obtained and stored as of the deployment of the link and be periodically compared against its up-to-date version, which may possibly contain anomalies. When the link becomes impaired, due to possible tilts, the faults can be visualized in an indicator map. We represent this anomaly detection scheme in Fig. 7b. Such methodology can also help automate the identification of anomalies in the link since the different faults leave unique "signatures" in the anomaly indicator map. For instance, a fiber excessive attenuation would leave a loss profile that is rather
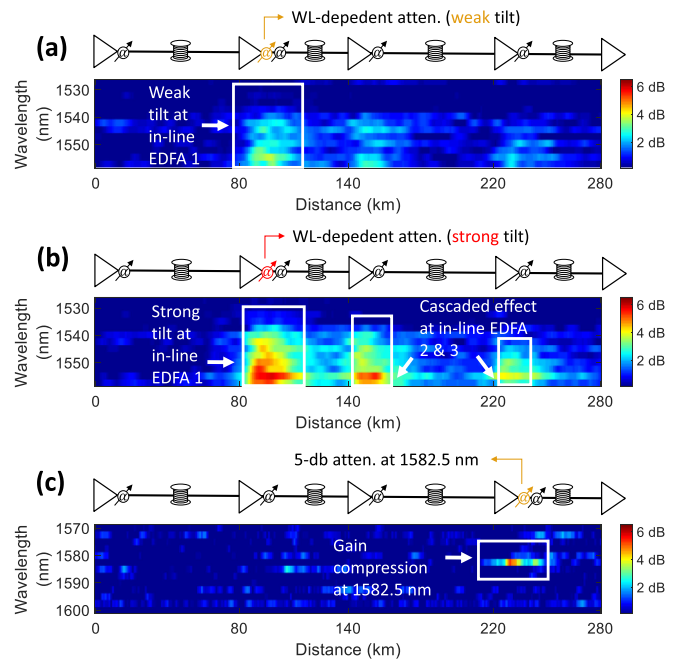

Fig. 8. Result of the anomaly indicator when a (a) Weak and (b) Strong tilt are emulated (for C-band) on the in-line EDFA 1 by adding a wavelength-dependent attenuation profile. In (c), the proposed anomaly detection scheme is used to visualize a 5-dB narrowband gain compression at 1582.5 nm, which emulates the effect of the SHB in the L-band.

constant along the wavelength axis (Fig. 7c), whereas the tilt will provoke an imbalanced loss profile that gradually varies with the wavelength (Fig. 7c).

To emulate tilts, we inserted a wavelength-dependent attenuator at the output of the AUT 1. This attenuator was programmed with two attenuation profiles (in the C-band from 1527.5 to 1557.5 nm). The first profile corresponds to a weak tilt (orange line in Fig. 7d) whereas the second profile is a strong tilt (red line in Fig. 7d). The b2b characterization of the AUT 1 without tilt (black circle-like markers), with weak tilt (orange circle-like markers) and strong tilt (red circle-like markers) are likewise displayed in Fig 7d.

As seen in Fig. 8a and 8b, the anomaly indicator map faithfully captures the two tested tilt profiles, which are denoted by the

gradual coloring of the heat map (stronger in Fig. 8b) along the wavelength axis. In Fig. 8b, it is also possible to visualize a strong cascaded effect at the in-line EDFA 2 and 3, caused by the tilt at the in-line EDFA 1, which becomes so severe that the subsequent amplifiers can no longer maintain a constant output power in the ACC mode.

Another important but less current impairment present in EDFAs can be caused by SHB. The SHB is characterized by the appearance of a very narrow dip in the spectrum, which causes a gain compression for a narrow wavelength range [24]. This effect can cause degradation of the channel's optical signal-to-noise ratio (OSNR) and severely impact the L-band transmission [25]. Similarly to the tilt case, the SHB is expected to leave a specific signature in the indicator map. This signature, illustrated in Fig. 7c, corresponds to a power disturbance limited to a very short wavelength interval, which represents the strong gain compression in that region. To verify whether the link tomography is able to successfully capture this fault, we used the same anomaly detection scheme in the tilt analysis. The difference is that now the anomalous link tomography is generated by adding a wavelength-dependent attenuator at the output of the in-line EDFA 3, which is programmed with a loss profile that is null from 1570 – 1600 nm, except at 1582.5 nm, where we induced a 5-dB notch. The result of the anomaly indicator is shown in Fig. 8c. In this new map, the gain compression is visible by the red coloring of the heat map for a very narrow wavelength interval at 1582.5 nm.

We suggest that computational tools based on Machine Learning can help automate classification and location of the studied faults. For instance, deep neural networks can be trained to predict from the anomaly indicator map the type of failure and possibly its location (space- and frequency-domain) [12].

V. CONCLUSION

In this work, we proposed the use of a receiver based DSP approach, i.e., the *in-situ* PPE, to construct a wavelength-wise, spatially-resolved link tomography that visualizes power evolution in C+L-band systems. Our results have experimentally demonstrated that this tool can be used to extract the spectral gain of EDFAs with a maximum mean absolute error of 0.6 dB in comparison to back-to-back characterization. Additionally, we investigated how the link tomography can be utilized to detect anomalies in the optical links, such as gain tilt and narrowband gain compression. We foresee that the link tomography can be used to detect tilts caused by stimulated Raman scattering due to power transfer from C- to L-band in a multi-channel scenario and to improve the accuracy of MB channel models by reducing the uncertainties of the wavelength-dependent fiber link parameters. As follow-up work, we believe that two alternative investigations are: (1) the performance validation of the link tomography in the presence of filtering effects induced by intermediate nodes; and (2) a possible extension of the *in-situ* PPE to account for heterogeneous multi-spans, once the

current version requires homogeneous properties throughout the link.

REFERENCES

[1] DataReportal, "Digital 2021 global digital overview," 2021. [Online]. Available: https://digital-2021-global-digital-overview-report

[2] A. Feldmann *et al.*, "Implications of the COVID-19 pandemic on the internet traffic," presented at the 15th ITG-Symp., 2021, pp. 1–5.

[3] V. Coffey, "Sea change: The challenges facing submarine optical communications," *OPTICA Opt. Photon. News*, vol. 25, no. 3, pp. 26–33, Mar. 2014.

[4] A. Ferrari *et al.*, "Assessment on the achievable throughput of multi-band ITU-T G.652.D fiber transmission systems," *IEEE/OPTICA J. Lightw. Technol.*, vol. 38, no. 16, pp. 4279–4291, Apr. 2020.

[5] J. Renaudier *et al.*, "107 Tb/s transmission of 103-nm bandwidth over 3×100 km SSMF using ultra-wideband hybrid Raman/SOA repeaters," presented at the Opt. Fiber Commun. Conf. Exhib., 2019, Paper Tu3F.2.

[6] R. Kraemer *et al.*, "Multi-band photonic integrated wavelength selective switch," *IEEE/OPTICA J. Lightw. Technol.*, vol. 39, no. 19, pp. 6023–6032, Oct. 2021.

[7] N. K. Fontaine, "36-THz bandwidth wavelength selective switch," presented at the Eur. Conf. Opt. Commun., 2021, Paper PD2.3.

[8] C. Doerr *et al.*, "O, E, S, C, and L band silicon photonics coherent modulator/receiver," presented at the Opt. Fiber Commun. Conf. Exhib., 2016, Paper Th5C.4.

[9] N. Sambo *et al.*, "Provisioning in multi-band optical networks," *IEEE/OPTICA J. Lightw. Technol.*, vol. 38, no. 9, pp. 2598–2605, May 2020.

[10] E. Seve, J. Pesic, C. Delezoide, S. Bigo, and Y. Pointurier, "Learning process for reducing uncertainties on network parameters and design margins," *IEEE/OPTICA J. Opt. Commun. Netw.*, vol. 10, no. 3, pp. A298–A306, Feb. 2018.

[11] E. Seve, C. Delezoide, J. Pesic, S. Bigo, and Y. Pointurier, "Automated fiber type identification," presented at the Eur. Conf. Opt. Commun., 2018, pp. 1–3.

[12] X. Chen, B. Li, R. Proietti, Z. Zhu, and S. J. B. Yoo, "Self-Taught anomaly detection with hybrid unsupervised/supervised machine learning in optical networks," *IEEE/OPTICA J. Lightw. Technol.*, vol. 37, no. 7, pp. 1742–1749, Apr. 2019.

[13] T. Tanimura, S. Yoshida, S. O. K.Tajima, and T. Hoshida, "Concept and implementation study of advanced DSP-based fiber-longitudinal optical power profile monitoring toward optical network tomography," *IEEE/OPTICA J. Opt. Commun. Netw.*, vol. 13, no. 10, pp. E132–E141, Oct. 2021.

[14] T. Tanimura, K. Tajima, S. Yoshida, S. Oda, and T. Hoshida, "Experimental demonstration of a coherent receiver that visualizes longitudinal signal power profile over multiple spans out of its incoming signal," presented at the Eur. Conf. Opt. Commun., 2019, pp. 1–4.

[15] T. Tanimura, S. Yoshida, K. Tajima, S. Oda, and T. Hoshida, "Fiber-longitudinal anomaly position identification over multi-span transmission link out of receiver-end signals," *IEEE/OPTICA J. Lightw. Technol.*, vol. 38, no. 9, pp. 2726–2733, May 2020.

[16] T. Sasai, M. Nakamura, E. Yamazaki, S. Yamamoto, H. Nishizawa, and Y. Kisaka, "Digital backpropagation for optical path monitoring: Loss profile and passband narrowing estimation," presented at the Eur. Conf. Opt. Commun., 2020, pp. 1–4.

[17] T. Sasai *et al.*, "Simultaneous detection of anomaly points and fiber types in multi-span transmission links only by receiver-side digital signal processing," presented at the Opt. Fiber Commun. Conf. Exhib., 2020, pp. 1–3.

[18] T. Sasai, M. Nakamura, T. Kobayashi, H. Kawakami, E. Yamazaki, and Y. Kisaka, "Revealing Raman-amplified power profile and raman gain spectra with digital backpropagation," presented at the Opt. Fiber Commun. Conf. Exhib., 2021, pp. 1–3.

[19] M. Sena, R. Emmerich, B. Shariati, J. K. Fischer, and R. Freund, "Link tomography for amplifier gain profile estimation and failure detection in C+L-band open line systems," presented at the Opt. Fiber Commun. Conf. Exhib., 2022, Paper Th1H.1.

[20] I. Miguel *et al.*, "Cognitive dynamic optical networks," *IEEE/OPTICA J. Opt. Commun. Netw.*, vol. 5, no. 10, pp. 107–118, Oct. 2013.

[21] K. Kaeval *et al.*, "QoT assessment of the optical spectrum as a service in disaggregated network scenarios," *J. Opt. Commun. Netw.*, vol. 13, no. 11, pp. E1–E12, 2021.

[22] T. Tanimura *et al.*, "Semi-blind nonlinear equalization in coherent multi-span transmission system with inhomogeneous span parameters," presented at the Opt. Fiber Commun. Conf. Exhib., 2010, pp. 1–3.

[23] J. Yu, S. Zhu, C. L. Gutterman, G. Zussman, and D. C. Kilper, "Machine-learning-based EDFA gain estimation," *IEEE/OPTICA J. Opt. Commun. Netw.*, vol. 13, no. 4, pp. B83–B91, Apr. 2021.

[24] M. Bolshtyansky, "Spectral hole burning in erbium-doped fiber amplifiers," *IEEE/OPTICA J. Lightw. Technol.*, vol. 21, no. 4, pp. 1032–1038, Jun. 2003.

[25] M. Sena *et al.*, "Performance evaluation of InP-based DP-IQ modulators for multiband transmission systems," presented at the Int. Conf. Transp. Opt. Netw., 2020, pp. 1–4.

[26] R. Emmerich *et al.*, "Enabling S-C-L-band systems with standard C-band modulator and coherent receiver using coherent system identification and nonlinear predistortion," *IEEE/OPTICA J. Lightw. Technol.*, vol. 40, no. 5, pp. 1360–1368, Oct. 2021.

[27] M. Sena *et al.*, "Bayesian optimization for nonlinear system identification and pre-distortion in cognitive transmitters," *IEEE/OPTICA J. Lightw. Technol.*, vol. 39, no. 15, pp. 5008–5020, Aug. 2021.

[28] D. Bayart, Y. Robert, P. Bousselet, J. Boniort, and L. Gasca, "Impact of spectral hole-burning for EDFAs operated in the long-wavelength band," *OPTICA Trends Opt. Photon.*, vol. 30, Jun. 1999, Paper WD5.